

# Alpha particle confinement metrics based on orbit classification in stellarators

Christopher G. Albert<sup>1†</sup>, Rico Buchholz<sup>1</sup>, Sergei V. Kasilov<sup>1,2,3</sup>,  
Winfried Kernbichler<sup>1</sup> and Katharina Rath<sup>4,5</sup>

<sup>1</sup>Fusion@ÖAW, Institute of Theoretical & Computational Physics, Graz University of Technology, 8010 Graz, Austria

<sup>2</sup>Institute of Plasma Physics, National Science Center “Kharkov Institute of Physics and Technology”, 61108 Kharkiv, Ukraine

<sup>3</sup>Department of Applied Physics and Plasma Physics, V.N. Karazin Kharkiv National University, 61022 Kharkiv, Ukraine

<sup>4</sup>Max Planck Institute for Plasma Physics, 85748 Garching, Germany

<sup>5</sup>Department of Statistics, Ludwig-Maximilians-Universität München, 80539 Munich, Germany

(Received xx; revised xx; accepted xx)

We present orbit classification schemes for use as fast metrics for fusion alpha particle losses implemented in the symplectic guiding-center code SIMPLE. Two variants respectively based on conservation of the parallel adiabatic invariant, and topology of footprints in Poincaré sections are introduced. Like an existing approach based on the Minkowski fractal dimension, those methods estimate whether a guiding-center orbit is regular and therefore expected to be confined for infinite time in the collisionless case, or chaotic, which might lead to its loss. Compared to the existing approach, the required orbit tracing time for the novel classifiers is shorter by at least an order of magnitude. This enables massive sampling of orbits across the whole phase space to identify regular and chaotic regions for the purpose stellarator optimization. Based on conservation of the perpendicular invariant, we demonstrate how extended regular regions may act as radial barriers for orbits from the chaotic regions on the radially inboard side. We propose to use a quantified version of this property as a new metric for collisionless fusion alpha losses. As pitch-angle scattering becomes only relevant after alphas have already deposited a significant fraction of their energy, such a metric remains useful also for the case with collisions. This is illustrated by comparison to collisional loss computations. Results are presented for applications to two quasi-isodynamic configurations, a quasi-helical configuration and two quasi-axisymmetric configurations. In addition, the Hamiltonian action-angle formalism is used in quasi-axisymmetric configurations to investigate the overlap of drift-orbit-resonances leading to chaos. The respective analysis is performed with the NEO-RT code originally developed for investigation of neoclassical toroidal viscous torque in tokamak plasmas.

## 1. Introduction

Minimizing the losses of fusion alpha particles is a major goal in the optimization of stellarator magnetic confinement configurations for self-heated fusion plasmas. Recent results (Paul *et al.* 2022; Landreman & Paul 2022; Landreman *et al.* 2022; Goodman *et al.* 2022) demonstrate that it is possible to achieve excellent fusion alpha confinement in

† Email address for correspondence: albert@tugraz.at

stellarator reactor configurations optimized towards precise quasisymmetry or quasiisodynamicity. Retaining this quality of alpha confinement while also fulfilling other objectives such as magnetohydrodynamic stability, low turbulent transport or coil complexity is a major challenge. Therefore, criteria for good alpha confinement that are more general than quasisymmetry and quasi-isodynamicity are still of high interest. Here we present and assess such criteria.

One way to obtain alpha loss fractions in a stellarator configuration consists in directly tracing guiding-center orbits with (optionally) the account of collisions via Monte Carlo operators. The slowing-down time of fusion alphas is in the range of 0.1-0.5 seconds. To decide whether a single guiding-center orbit remains confined during this time, typically requires tracing for  $> 10^4$  bounce periods. Numerical estimation of loss fractions from a statistical ensemble of  $10^4$  particles and hundreds of time-steps per period therefore requires billions of magnetic field evaluations. Despite recent acceleration by symplectic integration (Albert *et al.* 2020*b*) and Poincaré plot classification (Albert *et al.* 2020*a*; Kamath 2022), direct computation of alpha losses remains computationally expensive compared to other components of a stellarator optimization loop. While there has been recent progress on accelerating prompt loss computations (Velasco *et al.* 2021), there remains room for improvement of optimizing also late and collisional alpha energy losses.

For this purpose, two novel classifiers are introduced and their performance and reliability assessed on a test case in the optimized stellarator configuration of Drevlak *et al.* (2014). In the terminology of statistics, collisionless orbit classification checks the hypothesis whether a guiding-center orbit is lost by first testing the weaker hypothesis whether it is chaotic (potentially lost). This is done in a way analogous to a screening test for a disease. If a classifier wrongly identifies a regular orbit (never lost) as chaotic, this is known as a *false positive* or *type I error*. Another more accurate (and expensive) test will subsequently be required to come to a final conclusion. In our case, we directly check whether one of the pre-screened orbits deemed chaotic will be finally lost. More type I errors produce more (computational) cost, but the final result remains unchanged. In contrast, a wrong identification of a chaotic orbit as regular, is known as a *false negative* or *type II error*. In that case, the orbit is prematurely counted as confined, even though it may be lost later. While this kind of error must be avoided for exact final results, it may also be permissible as long as the error rate is sufficiently small, and the final error doesn't exceed statistical fluctuations. We compare two classifiers to the existing Minkowski classifier in terms of these error modes. The first classifier is based on topological properties of a subset of regular orbits in phase-space, and the other one on the variation of the parallel adiabatic invariant.

New classifiers are presented in section 2. Based on the increased computational performance of these classifiers, it becomes possible to analyze the regular and chaotic regions with a fine resolution across the whole phase space of collisionless fusion alpha orbits in a stellarator configuration in comparably short time. Such analyses are presented in section 3 for five optimized stellarator reactor configurations (Subbotin *et al.* 2006; Drevlak *et al.* 2014, 2018; Henneberg *et al.* 2019; Landreman & Paul 2022). The results are compared to direct computations of collisionless and collisional alpha particle and energy loss fractions from the guiding-center code SIMPLE (Albert *et al.* 2020*a,b*). Based on the quasi-axisymmetric case, the role of orbital resonances is pointed out, with more details described in a recent paper (Albert *et al.* 2022).

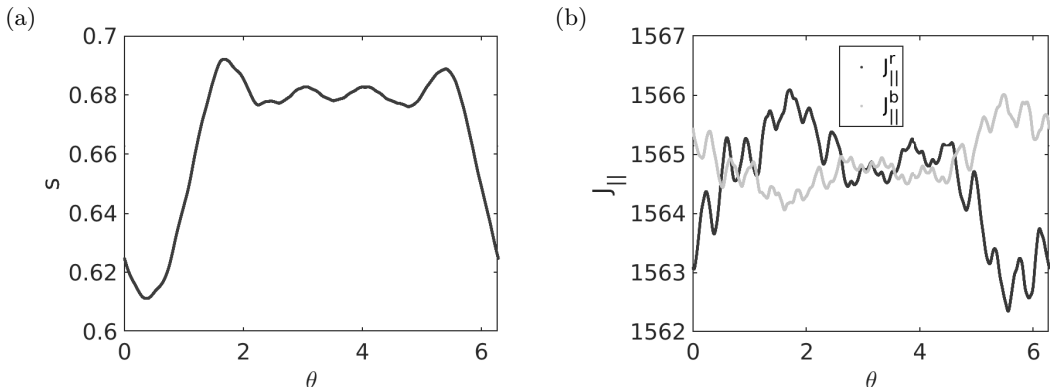


FIGURE 1. Poincaré plot of  $\approx 10,000$  footprints in  $(\theta, s)$  plane (left) and plot of  $(\theta, J_{\parallel})$  pairs for an “ideal” orbit of a 3.5 MeV alpha particle in the QI stellarator reactor configuration of Drevlak *et al.* (2014). First return invariant,  $J_{\parallel}^r$ , and bounce invariant  $J_{\parallel}^b$  are shown with black and gray dots, respectively.

## 2. Methods

Here we build on the idea of classification of collisionless orbits with help of Poincaré plots. In an earlier work (Albert *et al.* 2020a), distinguishing *regular* and *chaotic* orbits has been based on box-counting as an estimate of the Minkowski fractal dimension. This method required about 8000 footprints in a Poincaré plot to work reliably. Our aim is to devise alternative algorithms which will distinguish regular trapped orbits from chaotic ones using a much lower number of footprints.

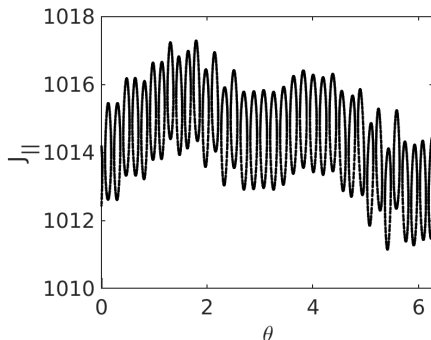
We start from *ideal* orbits, which approximately follow poloidally closed contours of the parallel adiabatic invariant  $J_{\parallel}$  in quasi-isodynamic (QI) configurations (Gori *et al.* 1996). We call them “ideal” because all orbits should be like this in a perfect QI configuration. The same definition of ideal orbits applies also to the quasi-helical (QH) configuration but not to the quasi-axisymmetric (QA) configuration where the symmetry direction is toroidal, and, therefore, contours must be closed toroidally, not poloidally. Up to this change, the results for QI configurations apply also to QA configurations. Regular orbits are a superset of ideal orbits, as their footprints are required to lie on closed curves which are not necessarily single-valued functions of the relevant angle.

An example Poincaré plot of the banana tips (Poincaré cut is a hypersurface  $v_{\parallel} = 0$  with  $v_{\parallel}$  changing sign from negative to positive) of an ideal orbit in QI configuration is shown in Fig. 1 in the  $(\theta, s)$  plane where  $s$  is a flux surface label and  $\theta$  is a poloidal angle. If  $\theta$  is an angle in quasisymmetry direction (toroidal angle in case of QA configurations), and quasisymmetry is perfect, banana tips of any orbit lay on a curve  $s(\theta) = \text{const}$  and therefore all orbits are ideal. Also in this figure, the lowest order parallel adiabatic invariant  $J_{\parallel}$  is shown that has been computed in two ways as follows:

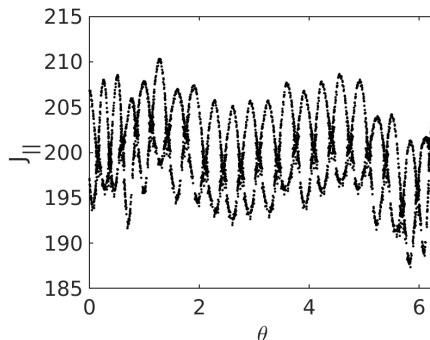
$$J_{\parallel}^r = \int_0^{\tau_r} dt v_{\parallel}^2, \quad J_{\parallel}^b = \lim_{\rho_L \rightarrow 0} \int_0^{\tau_b} dt v_{\parallel}^2, \quad (2.1)$$

The “first return” invariant  $J_{\parallel}^r$  is computed along the real orbit with finite Larmor radius (FLR) as an integral of the squared parallel velocity  $v_{\parallel}^2$  over the return time to the Poincaré cut  $\tau_r$  i.e. along the orbit connecting two subsequent footprints. The “bounce” invariant  $J_{\parallel}^b$  is computed the usual way, along the field line, i.e. in the limit of zero Larmor radius  $\rho_L$ . In the latter approximation, the orbit is closed within a bounce

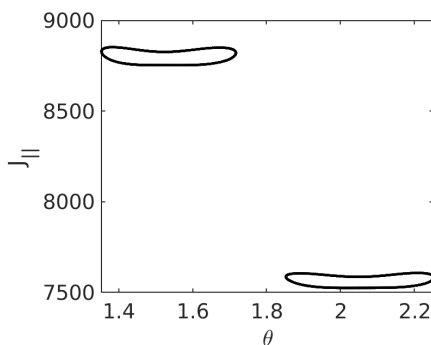
(a) trapped in drift-orbit resonance



(b) near separatrix of resonance



(c) transient regular



(d) transient chaotic

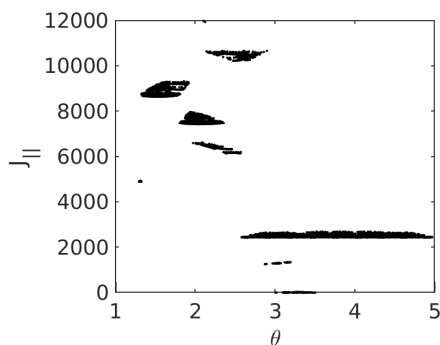


FIGURE 2. Examples of “non-ideal” orbits for 3.5 MeV alphas in the QI configuration of Drevlak *et al.* (2014) started from flux surface  $s = 0.6$ . Orbits non-linearly trapped in a resonance (a) and some transient orbits (c) are regular and therefore confined. In contrast, orbits close to a resonance separatrix (b) and transient chaotic orbits (d) are possibly lost.

time  $\tau_b$  which differs from  $\tau_r$  by first order terms in Larmor radius, unless the FLR orbit undergoes a transition. It can be seen that our “ideal” orbit actually does not follow exactly the contours of neither of these two. Although the changes in lowest order  $J_{\parallel}$  are within the fourth digit, they are of the same order for both definitions. Actually, this variation is because lowest order  $J_{\parallel}$  differs from the exact invariant by the first order terms in Larmor radius (Hastie *et al.* 1967). We will use this property later to introduce a classification method based on the relative variation in  $J_{\parallel}$ .

Despite small variations in  $J_{\parallel}$ , it is clearly seen in Fig. 1 that all the footprints are located on a smooth curve  $s = s(\theta)$  - the cross-section of the KAM surface (“drift surface”) by the Poincaré cut  $v_{\parallel} = 0$ . This curve is an invariant manifold of the Poincaré map, each mapping maps this curve onto itself, but the points get displaced along the curve. Let us use this property for orbit classification. According to Poincaré recurrence theorem, an orbit performing motion within a closed volume returns to any small vicinity of the starting point after a finite time,  $\tau_R$ , which depends on the size of this vicinity, and it does this subsequently an infinite number of times. Besides the vicinity size, the recurrence time  $\tau_R$  depends also on the type of the orbit. For the ideal regular orbits as the one shown above it has a near-periodic property which we discuss and use below.

Figure 2 shows a comparison of different types of non-ideal orbits. The orbits on the left side (non-linearly trapped in a resonance and transient regular orbit) are regular and

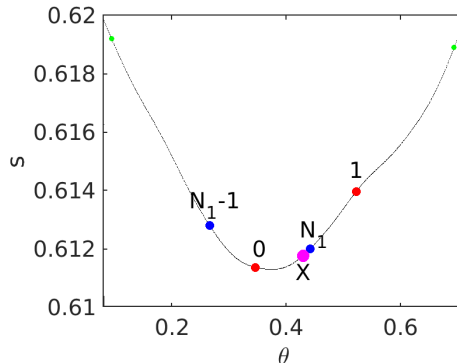


FIGURE 3. First two (red) and last two (blue) footprints of the mapping completing the first recurrence. The point  $X$  is plotted in magenta.

therefore absolutely confined despite being non-ideal. The orbit trapped deeply in a drift-orbit resonance (see section 3.1) is similar to the non-ideal orbits shown below in Fig. 4. Such orbits appear as narrow island chains and are thus prone to mis-classification due to their similarity to ideal orbits and relatively low variations in the parallel invariant. In contrast, the footprints of regular transient orbits (orbits whose number of local field minima traversed over the first return time  $\tau_r$  changes during the precession) switch between distinct islands in phase-space. Since trapped resonant orbits and transient regular orbits are both regular, mis-classification does not affect final results for losses. Other non-ideal orbits (near separatrix of resonance and transient chaotic) are potentially lost and have to be traced until their slowing down time in calculations of loss statistics.

### 2.1. Topological orbit classifier

We now want to develop the first idea used to classify orbits based on the already mentioned near-periodic property of the recurrence time  $\tau_R$  for ideal orbits. Let us first enumerate subsequent footprints  $(\theta_k, s_k)$  starting from  $k = 0$  and fix the interval  $\theta_0 < \theta < \theta_1$  between the first two footprints. An orbit will return to this interval after  $N_1$  mappings, where  $N_1$  is the first recurrence number. Subsequent recurrence numbers  $N_j$  are defined such that  $\theta_0 < \theta_{N_j} < \theta_1$ . For an “ideal” orbit, all  $N_j$  are inside the interval  $N_1 - 1 \leq N_j - N_{j-1} \leq N_1$ . The proof is apparent from Fig. 3. The segment of the invariant line between the initial two footprints 0 and 1 is mapped onto the segment between footprints  $N_1 - 1$  and  $N_1$  after  $N_1 - 1$  Poincaré mappings. By a continuity argument, there exists a point  $X$  within the original segment  $[0 : 1]$  which is mapped exactly onto point 0 after  $N_1 - 1$  mappings. Therefore, all points of the segment  $[0 : 1]$  located between points  $X$  and 1 are mapped onto the sub-segment between points 0 and  $N_1$  performing a recurrence after  $N_1 - 1$  mappings. Points located between points 0 and  $X$  are mapped onto the sub-segment between points  $N_1 - 1$  and 0. The latter points require one more mapping in order to arrive in a sub-segment between points  $N_1$  and 1. These points perform a recurrence after  $N_1$  mappings. Thus, if  $N_{j-1}$  is a recurrence number  $j-1$  such that  $\theta_0 < \theta_{N_{j-1}} < \theta_1$ , the next recurrence number will be either  $N_j = N_{j-1} + N_1 - 1$  or  $N_j = N_{j-1} + N_1$ , so that both cases satisfy  $N_1 - 1 \leq N_j - N_{j-1} \leq N_1$  with  $j \geq 2$ .

By a similar argument, each second recurrence satisfies  $N_2 - 1 \leq N_{2k} - N_{2(k-1)} \leq N_2$  with  $k \geq 2$ , and, more generally, each  $n$ -th recurrence satisfies

$$N_n - 1 \leq N_{nk} - N_{n(k-1)} \leq N_n, \quad (2.2)$$

---

	precessions	class	Minkowski	
			regular	chaotic
topological	2	ideal	307	20
		non-ideal	6	50
	4	ideal	302	8
		non-ideal	11	62
	8	ideal	296	3
		non-ideal	17	67
	16	ideal	289	2
		non-ideal	24	68
	32	ideal	285	1
		non-ideal	28	69
	128	ideal	277	0
		non-ideal	36	70

---

TABLE 1. Comparison of classification by Minkowski dimension and by topological classification using a simple recurrence relation.

---

with  $k \geq 2$ . Note that a recurrence  $N_j$  approximately corresponds to  $j$  poloidal precession turns (the higher  $j$ , the more accurate is this relation). Therefore, prompt orbit losses occur within the first recurrence.

The simplest algorithm to detect ideal orbits using recurrence (2.2) for  $n = 1$  is then straightforward. Every orbit is followed over  $M$  precession turns, and after each turn  $j$  a recurrence number  $N_j$  is checked to be within  $N_1 - 1 \leq N_j - N_{j-1} \leq N_1$ . If this condition is fulfilled for all  $M$  precession turns, an orbit is classified as “ideal”. Otherwise, it is classified as “non-ideal”. The results of this classification are compared to classification using Minkowski dimension in Tab. 1. The table compares the classification of the orbits for different numbers of precession turns.

As not all regular orbits are ideal, but all ideal orbits are regular, the topological classifier may correctly identify a regular orbit as non-ideal (Fig. 2). This does not lead to errors in the directly computed collisionless alpha loss result using the topological classifier for speed up, but only increases computation time, as non-ideal/chaotic orbits are traced to the end. In contrast, an orbit wrongly identified as ideal by the topological classifier leads to an underestimation of losses.

In the absence of errors, all chaotic orbits should be identified as non-ideal, however this is not immediately the case. It can be seen that chaotic orbits wrongly counted as ideal by the topological classifier disappear after 16-32 precession turns. However, depending on the number of precession turns, some non-ideal, regular orbits are identified as ideal. While this doesn’t affect prediction of losses, it should be kept in mind for applications where this distinction is important.

The single remaining mismatch after 32 turns in Tab. 1 has been manually identified as a simultaneous mis-classification of a regular non-ideal orbit due to a *type I* error by the Minkowski method and a *type II* error by the topological classifier, see Fig. 4. With larger sample sizes, an accurate classifier might require 128 turns. We have used this number here to demonstrate how the classification results stabilize when going towards a “large” number of footprints. The number of footprints for one turn is about 40, therefore one may require up to 4000 footprints – not much less than for the Minkowski classifier. If one decides to tolerate some mis-classification, note that for 8 turns, there are still 3

	precessions	class	Minkowski	
			regular	chaotic
topological	2	ideal	307	20
		non-ideal	6	50
	4	ideal	291	3
		non-ideal	22	67
	8	ideal	281	1
		non-ideal	32	69
	16	ideal	271	1
		non-ideal	42	69
	32	ideal	265	0
		non-ideal	48	70
	128	ideal	258	0
		non-ideal	55	70

TABLE 2. Comparison of classification by Minkowski dimension and by using the topological classifier with multiple recurrence and monotonicity criteria.

unidentified orbits (error around 1%). As expected, some orbits classified as regular by Minkowski dimension are “non-ideal” in the recurrence classification. Those orbits cannot be “ideal” orbits because ideal orbits in this algorithm can be misclassified only due to numerical errors which are at the level of computer accuracy in our case.

The simplest topological classification algorithm may be improved in two ways. First, by checking relations (2.2) for all possible  $n$  values which are allowed by the condition  $2n < M$ , so that recurrence with the maximum  $n$  value is checked at least once. Second, one may additionally check the monotonicity of the ordered footprint sequence described below.

Let us order the recurrence numbers  $N_1, N_2, \dots, N_M$  in the increasing sequence with respect to  $\theta$ . Namely, we order their indices  $j = j_k$  where  $k = 1, 2, \dots, M$  so that  $\theta_0 < \theta_{N_{j_1}} < \theta_{N_{j_2}} < \dots < \theta_{N_{j_M}} < \theta_1$ . For an ideal orbit, this sequence is kept in all intervals between the subsequent footprints,

$$\theta_0 < \theta_{N_{j_1}} < \theta_{N_{j_2}} < \dots < \theta_{N_{j_M}} < \theta_1 \Rightarrow \theta_k < \theta_{N_{j_1}+k} < \theta_{N_{j_2}+k} < \dots < \theta_{N_{j_M}+k} < \theta_{k+1}, \quad (2.3)$$

where  $k \geq 1$ , and we assume no periodic boundaries within intervals  $[\theta_k, \theta_{k+1}]$ . Condition (2.3) obviously follows from mapping of the continuous segment  $[\theta_0, \theta_1]$  onto the segment  $[\theta_k, \theta_{k+1}]$  after  $k$  mappings in case the cross-section of the KAM surface is a simply connected line defined by some single valued function  $s = s(\theta)$ . We apply this additional restriction to the orbits which have been qualified as “ideal” by the improved (multiple) recurrence classification, in order to remove further type II errors.

The result of additional classification using the monotonicity condition (2.3) is compared to classification by Minkowski dimension in Tab. 2. It can be seen that all chaotic orbits are sorted out by this criterion already after 8 precession turns (the remaining orbit is, as we remember, a mis-classification by the Minkowski dimension). A manual study of the first 47 orbits classified by monotonicity condition as “ideal” shows that indeed, most of them are ideal, like the first orbit in Fig. 4. There are only two exceptions of the type shown in the lower panel of Fig. 4. These two orbits are re-classified as non-ideal after 32 precession turns.

The error mode is shown in Fig. 5 where an orbit close to the periodic orbit (invariant

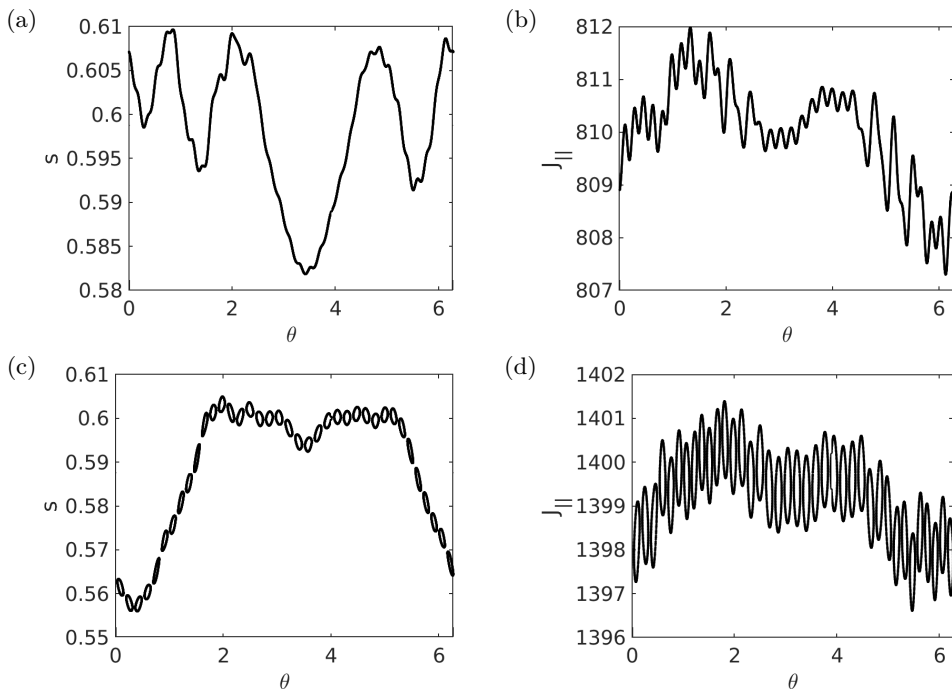


FIGURE 4. Poincaré plots in  $(\theta, s)$  (left) and  $(\theta, J_{||})$  (right) planes for two regular orbits classified as “ideal” by condition (2.3). A typical ideal and therefore regular orbit is shown in the upper panel, and a *type I* mis-classification by Minkowski dimension of a regular but non-ideal orbit is shown in the lower panel.

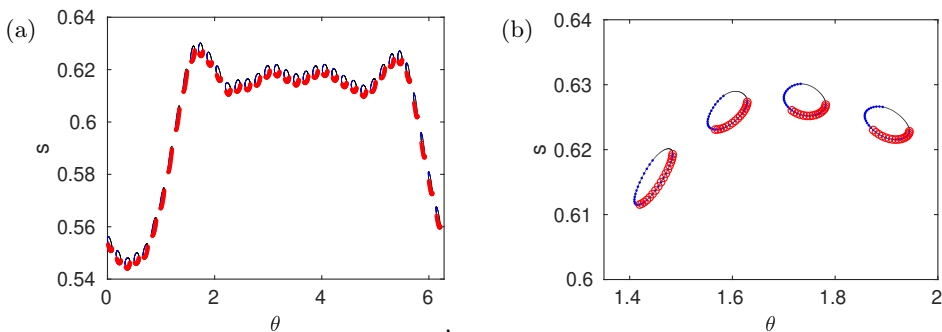


FIGURE 5. Example of a regular non-ideal orbit that is mis-classified as ideal by the topological classifier (zoomed view to the right). First 609, 1217 and 8918 footprints are plotted with red circles, blue and black dots, respectively.

axis) is plotted for 16, 32 and a much larger number of precession turns resulting in 609, 1217 and 8918 footprints, respectively. With 16 precession turns, the orbit is wrongly identified as ideal by both, recurrence and monotonicity conditions. For 32 turns, the version with multiple recurrence and monotonicity, Eq. (2.3), becomes correct, while using simple recurrence alone still leads to a mis-classification.

## 2.2. Parallel invariant classifier

A different classification method relies on the approximate conservation of the parallel adiabatic invariant  $J_{||} = J_{||}^r$ . As we have seen, for the ideal orbits and island-type orbits



	precessions	class	Minkowski	
			regular	chaotic
$J_{\parallel}$	2	regular	305	3
		chaotic	8	67
	4	regular	305	1
		chaotic	8	69
	8	regular	305	1
		chaotic	8	69

TABLE 3. Comparison of classification by Minkowski dimension and by using  $J_{\parallel}$ . No more changes appear for more than 4 precessions, up to at least 128 precessions.

resulting from nonlinear trapping into the drift orbit resonance, variation of  $J_{\parallel}$  is rather small, below 1%. More generally, also for most of non-ideal but regular orbits, the relative variations in  $J_{\parallel}$  remain small. Exceptions are regular transient orbits (Fig. 2c) which are rather rear. This is why this classifier may be used to distinguish regular from chaotic orbits, rather than ideal from non-ideal ones.

Here we have implemented classification with lowest order  $J_{\parallel}$  via a condition of regular orbits

$$|J_{\parallel}^{(k)} - J_{\parallel}^{(1)}| < \Delta J_{\parallel}, \quad (2.4)$$

where  $J_{\parallel}^{(k)}$  are the values of  $J_{\parallel}^r$  defined by Eq. (2.1) for the first return period starting from footprint number  $k$ . The result of classification using the condition (2.4) with  $\Delta J_{\parallel}$  chosen as 1% of its initial value is shown in Table 3. It can be seen, that starting from 4 precession turns the result of classification does not change, and only one chaotic orbit according to Minkowski dimension is classified as regular by  $J_{\parallel}$  (this orbit is the same regular orbit mis-classified by Minkowski dimension above). It can also be seen that there are 8 regular orbits classified by condition (2.4) as chaotic. All these are regular transient orbits (see Fig.2c) constituting less than 3% of all regular orbits.

### 2.3. Summary of classification

Up to now, we have introduced two disjoint pairs of orbits classes: *regular/chaotic* and *ideal/non-ideal*. Ideal orbits are a subset of regular orbits, but non-ideal are not necessarily chaotic. Besides that, a common classification splits the trapped particle population into *transient/non-transient*. As mentioned above, transient means that an orbit jumps between trapping classes during its precession, thereby abruptly changing its  $J_{\parallel}$  value. (Here, the trapping class is determined by the number of local minima traversed over one bounce time.) Note, that in the bounce-averaged approximation (Velasco *et al.* 2021), *only* transient orbits appear as chaotic. In the full guiding-center model, where the bounce phase is retained, transient orbits can not only be chaotic, but also regular. At the same time, ideal orbits are never transient. A graphical summary of this taxonomy with reference to examples is given in Fig. 6.

From the analysis above we can conclude that in the considered test case in the QI configuration of Drevlak *et al.* (2014), classification by  $J_{\parallel}$  is more accurate than by Minkowski dimension with the current settings and much faster: It requires 4 precession turns i.e. about 100-150 footprints in contrast to near 10000 footprints needed for the Minkowski dimension. The topological classifier with monotonicity reaches similar performance. A disadvantage of the  $J_{\parallel}$  classifier is that the threshold has to be set by

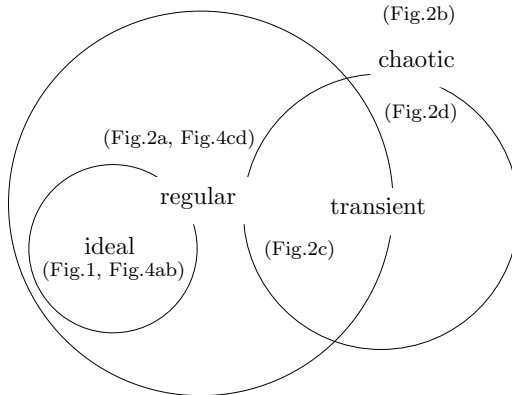


FIGURE 6. Taxonomy of orbits. Disjoint sets regular/chaotic, ideal/non-ideal and transient/non-transient are shown with their overlap and reference to example figures. The outermost region are chaotic non-transient orbits.

hand based on empirical data. Despite recognizing some non-ideal regular orbits, transient regular orbits are still classified as chaotic by the  $J_{\parallel}$  criterion. The topological classifier only recognizes the subset of ideal orbits as regular, and thus requires more orbits to be traced to the end. In turn, when converged, the topological classifier requires no manual tuning.

It should be noted that a classification without errors by any method would require tracing orbits over infinite time. The main problem is presented by orbits close to periodic orbits (invariant axes, where the footprints are mapped onto themselves after a finite number of returns). According to the Poincaré-Birkhoff theorem (?) such orbits exist everywhere in the phase volume, including ergodic regions. Such regular orbits have very low rotational transform if they are close to an invariant axis. Thus a classifier can easily confuse them with ideal orbits, if the tracing time is too short. This behavior is shown in Fig. 5. The closer an orbit is to an invariant axis, the longer it takes to correctly classify it. The same is true for chaotic orbits. In contrast to regular orbits, chaotic orbits depart from an invariant axis according to an exponential law (Lyapunov exponent). This departure can still be slow if they start very close to the axis. This can lead to a mis-classification as regular, but fortunately, the amount of these orbits is exponentially small.

### 3. Results and discussion

Figs. 7-12 show the results from SIMPLE in the two new classifier modes as well as the collisional mode for five optimized stellarator reactor configurations (Subbotin *et al.* 2006; Drevlak *et al.* 2014, 2018; Henneberg *et al.* 2019; Landreman & Paul 2022). For each configuration, classification runs are performed for 500.000 collisionless trapped alpha orbits started from banana tips ( $v_{\parallel} = 0$ ) randomly distributed in plasma volume. Classification results are scored on the rectangular  $50 \times 300$  grid in starting banana tip radius  $s$  and the normalized perpendicular invariant,  $J_{\perp}$  which takes values ranging from zero for strongly passing orbits to 1 for orbits deeply trapped at the global magnetic field minimum. As a result, each grid cell contains  $N_g$  good (ideal or regular, depending on classifier),  $N_a$  average (non-ideal or chaotic) and  $N_b$  bad (promptly lost) orbits. The predominant orbit class  $C$  defined via these numbers as

$$C = (N_g - N_b)/(N_g + N_a + N_b) \quad (3.1)$$

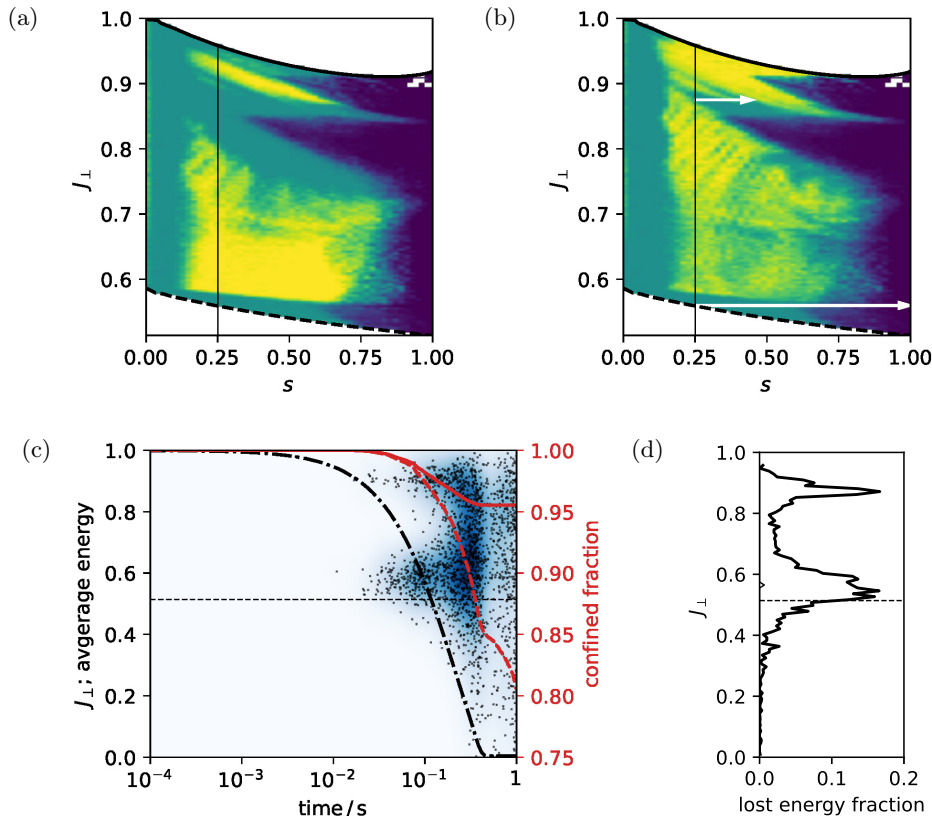


FIGURE 7. Quasi-isodynamic configuration of Subbotin *et al.* (2006). (a-b) show on an  $(s, J_\perp)$  grid the predominant orbit class (3.1) in the trapped region bounded from above (deeply trapped —), and from below (trapped-passing boundary —). Thin vertical lines at  $s = 0.25$  mark starting flux surface for loss computation in (c-d).

(a)  $J_\parallel$  classification. Colormap for predominantly regular (bright), chaotic (medium) and promptly lost (dark) orbits.

(b) Analogous to (a) for topological classification with ideal (bright), non-ideal (medium) and promptly lost (dark).

(c) Left axis:  $J_\perp$  for lost particles marked by dots and estimated loss distribution over time. Normalized average kinetic energy (—) of slowing-down particles. Right axis (red): Collisional confined fraction of particles (—) and energy (—) over time.

(d) Final lost energy fraction over  $J_\perp$  for collisional (thick line) and collisionless (thin line) alpha particles. This configuration shows only minimal collisionless losses near  $J_\perp = 0.55$ . This loss channel is marked by a white arrow in (b). Another loss channel near  $J_\perp = 0.9$  is blocked for collisionless orbits, but not if collisions change  $J_\perp$  over time. Thin dashed lines in (c-d) mark the minimum  $J_\perp$  value from (a-b).

is shown as a colored pixel on this grid. Orbits are classified as promptly lost if they leave the confinement region before a criterion can be computed. If they reach this point, in the case of the  $J_\parallel$  criterion, orbits are counted as regular, if the relative variation in  $J_\parallel$  is below 1%. Otherwise, they are counted as chaotic. For the topological classifier, orbits are counted as ideal if they fulfil the according recurrence and monotonicity criteria, and non-ideal otherwise.

To interpret the classification plots in the upper part of Figs. 7-12 it is important to recall from section 2 that, independently of the chosen thresholds, there exist regular non-

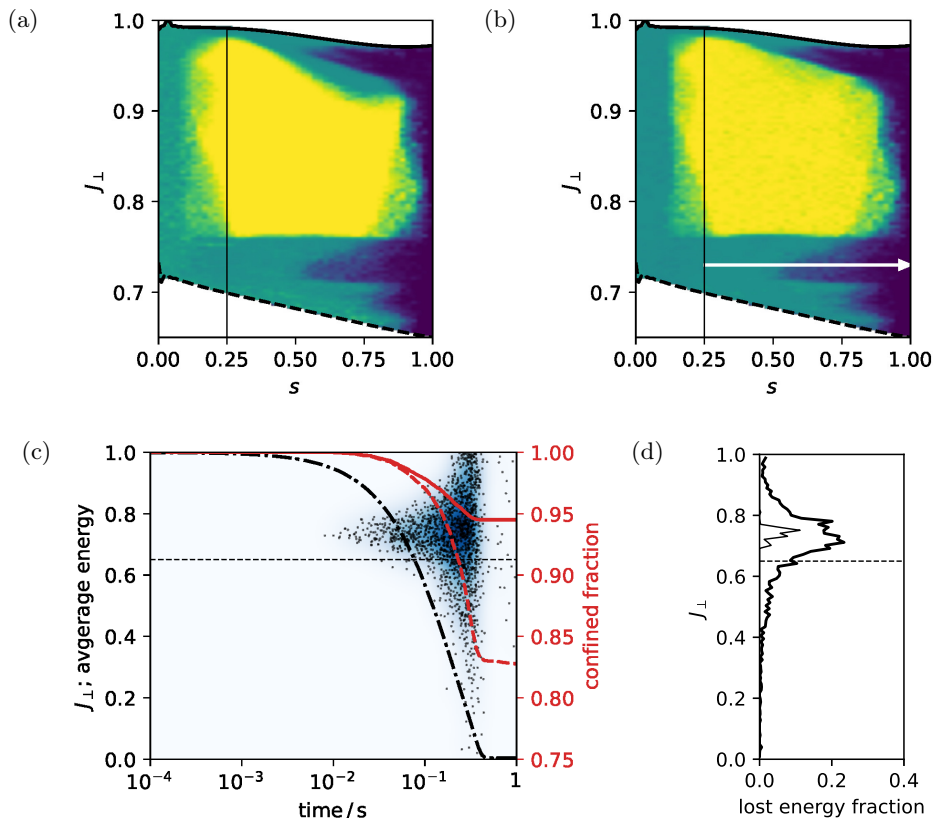


FIGURE 8. As Fig. 7, but for the QI configuration of Drevlak *et al.* (2014). Here, non-ideal orbits and losses extend over a region at the trapped-passing boundary near normalized  $J_{\perp} = 0.7$ . The total collisional energy loss fraction slightly above 5% matches the one of Drevlak *et al.* (2014), where starting distribution and plasma profiles have been modeled in more detail.

ideal orbits. If the classifier makes no error, there exist however no chaotic ideal orbits. Completely regular regions and thus their subset of ideal regions guarantee collisionless confinement. Furthermore, collisionless orbits move on contours of constant  $J_{\perp}$ . This means that whenever there exists a regular region with the same  $J_{\perp}$  at a radius outside the initial position, this region will block the orbit from escaping. In the graphical representation interpreted as a projection in phase-space this means that orbits may only evolve in the horizontal direction. Thus, regular/ideal regions plotted in bright yellow act as loss barriers. For the purpose of optimizing a stellarator configuration in terms of chaotic alpha losses, it should be sufficient to “pin down” such barriers by maximizing the fraction of regular or better ideal orbits on a few flux surfaces, e.g. at  $s = 0.25$  and  $s = 0.5$ . The reason why ideal orbits are preferable to just regular ones will become clear below. From the computing time required for the present global analysis with the topological method, this should be feasible in a few minutes of computing time on a single cluster node and can be parallelized further easily.

### 3.1. The role of orbital resonances

Fig. 11 is a special case to demonstrate the difference of lower-energy orbits of 35 keV to alpha orbits at 3.5 MeV in Fig. 10. At lower energy, the orbit width decreases, and

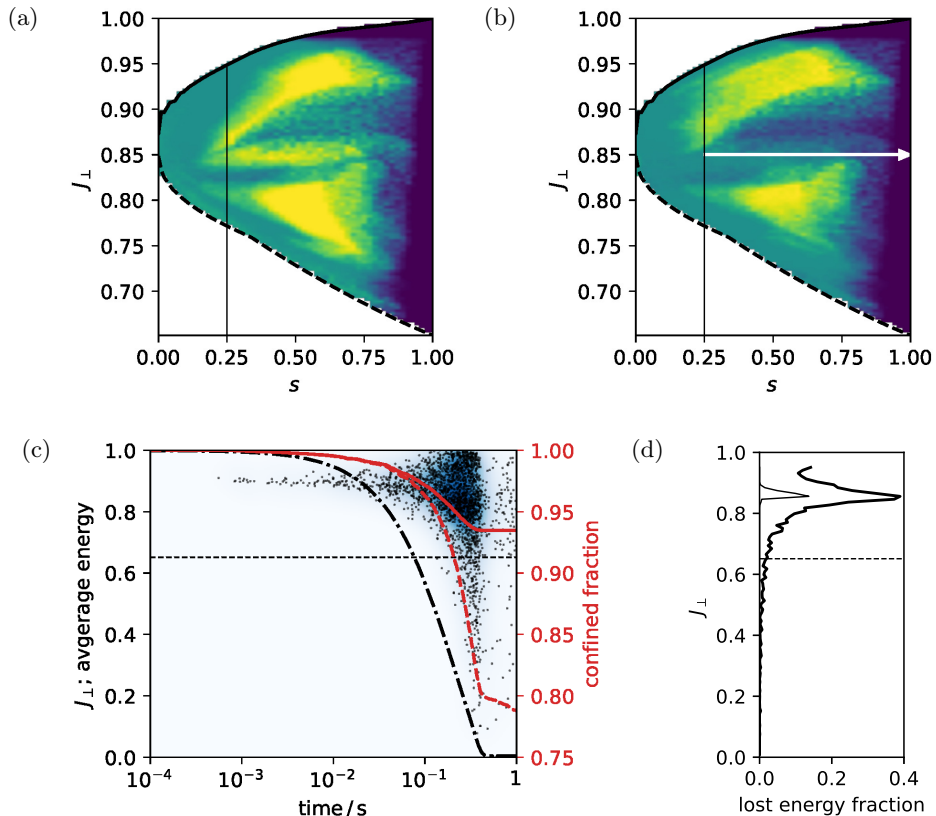


FIGURE 9. As Fig. 7, but for the QH configuration of Drevlak *et al.* (2018) with alpha losses via a region of non-ideal orbits around normalized  $J_{\perp} = 0.85$ .

the ideal orbit criterion converges towards the criterion of closed  $J_{\parallel}$  contours (Gori *et al.* 1996) in the limit of infinitesimal orbit width. The latter criterion is valid for thermal ions and usually fulfilled in a large fraction of phase-space for devices close to omnigenity (QI, QH and QA). In contrast, for energetic fusion alphas at 3.5 MeV, no predominantly ideal regions, and few regular regions exist in this example. This behavior is understood in terms of overlapping drift-orbit resonances computed in the code NEO-RT (Albert *et al.* 2016, 2022) plotted in Fig. 13. An orbital resonance occurs whenever canonical bounce frequency  $\omega_b$  and toroidal precession frequency  $\Omega_t$  fulfil the condition

$$m_2\omega_b(\mathbf{J}) + m_3\Omega_t(\mathbf{J}) = 0 \quad (3.2)$$

with integer harmonics  $m_2$  and  $m_3$  in canonical angle variables. This resonance is defined in the perfectly symmetric limit with three invariants of motion  $\mathbf{J}$  – in this case quasi-axisymmetry. The special case  $m_2 = 0$  where the orbit doesn't precess toroidally is called a superbanana resonance. Generally, in a configuration close to perfect symmetry (it can also be a “hidden” one), orbits perform non-linear oscillations around such resonances that appear as island chains in Poincaré plots (non-ideal, see Fig. 2a-b). The amplitude of these oscillations is known as the resonance width, and grows quadratically with the amplitude  $H_m$  of the Hamiltonian perturbation  $\delta H$  in Fourier harmonics for canonical

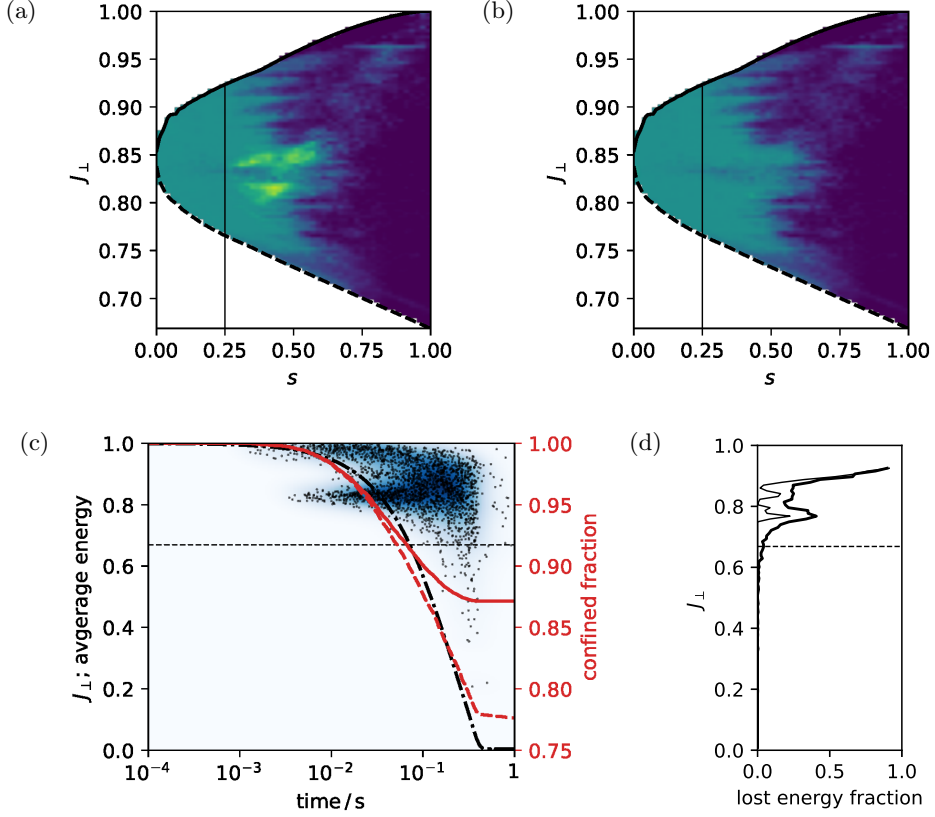


FIGURE 10. As Fig. 7, but for the QA configuration of Henneberg *et al.* (2019). Most trapped orbits are chaotic due to resonance overlap shown in Fig. 13a), or promptly lost. Two regions with a larger fraction of regular but non-ideal orbits block some losses.

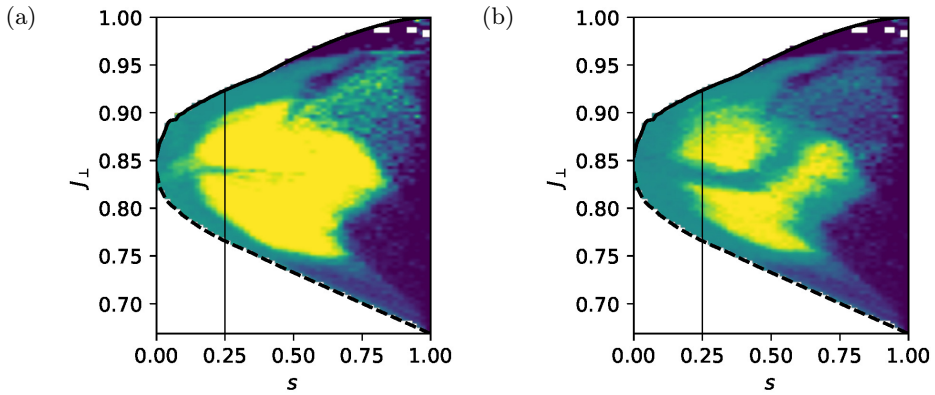


FIGURE 11. As Fig. 10(a,b) but with particle energy reduced by factor 100 (35 keV alphas). Compared to Fig. 10, larger regular/ideal regions are visible. A non-ideal region is visible around the superbanana resonance in Fig. 13b).

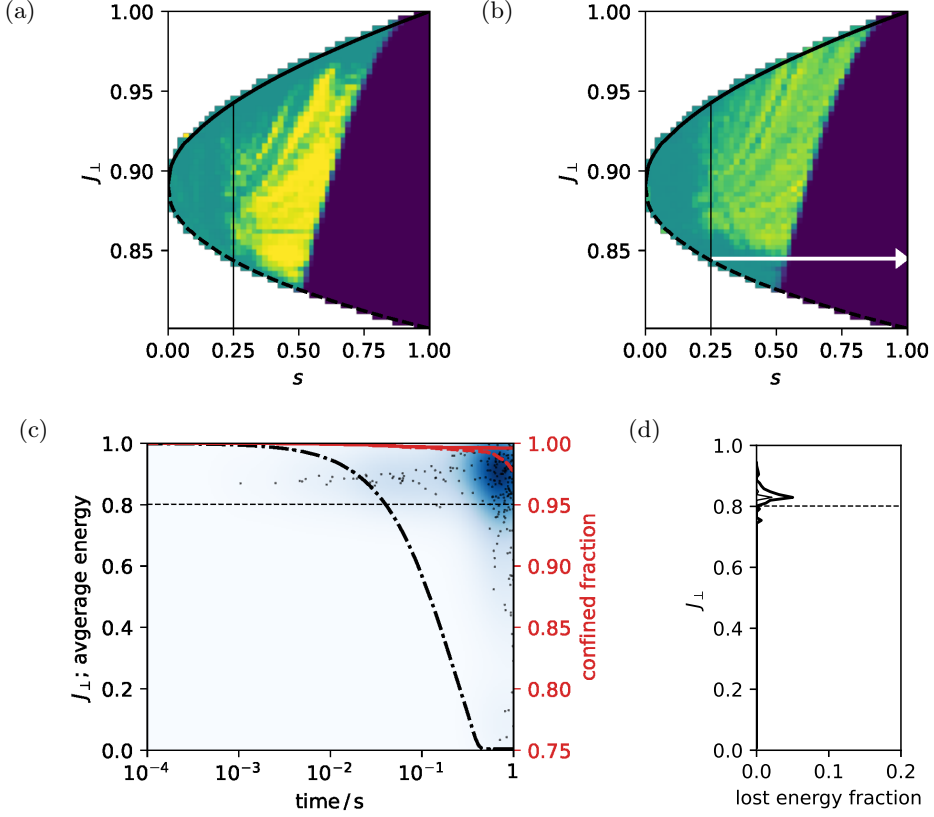


FIGURE 12. Quasi-axisymmetric configuration of Landreman & Paul (2022) as in Fig. 7. The resonance structure matches Fig. 13c) and the small deviation from quasisymmetry prevents resonance overlap and therefore chaos. Prompt losses at  $s \geq 0.5$  are from wide banana orbits.

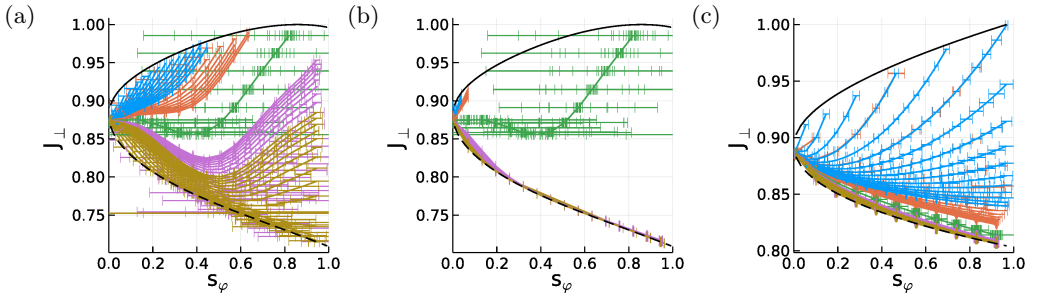


FIGURE 13. Orbital resonance lines (Albert *et al.* 2022) for QA configurations from (a) Fig. 10, (b) Fig. 11 and (c) Fig. 12 in the thin orbit limit of NEO-RT (Albert *et al.* (2016), precise values of  $J_{\perp}$  and shape of resonances may differ from full orbits). Colors indicate different canonical bounce harmonics, and error bars show the linear resonance width.

angles (Albert *et al.* 2016, 2022). In our case the perturbation scales linearly with non-quasisymmetric part  $\delta B = B - B_0$  of the magnetic field module,

$$\delta H = (\omega_{c0} J_{\perp} + m_{\alpha} v_{0\parallel}^2) \frac{\delta B}{B_0} = H_0 \left( 1 + \frac{m_{\alpha} v_{0\parallel}^2}{2H_0} \right) \frac{\delta H}{B_0}, \quad (3.3)$$

where quantities with subscript “0” refer to their quasisymmetric part.

Once the resonance width becomes of the order of the distance between resonances, chaotic phase-space regions appear in-between. The degree of overlap is measured by the Chirikov criterion (Chirikov 1979). Intact KAM surfaces in-between island chains of resonances prevent crossing of chaotic orbits and are identified as footprints of ideal orbits.

For full alpha energy in Fig. 11, most orbital resonances overlap and produce global chaos. At reduced energy, only the superbanana resonance remains. Non-linear oscillations around this resonance can be seen in the form of regular but non-ideal orbits in Fig. 11b). Further away from the resonance line on the inboard side, one may even notice a region of prompt losses arising from non-linear oscillations around the resonance over a radial region that crosses the plasma boundary  $s = 1$ . Such orbits are barely trapped in the resonance and perform wide oscillations over both,  $J_{\parallel}$  and  $s$  (Fig. 2b). Also a comparison of the second QA configuration in Fig. 12 with Fig. 13c) shows a banded structure for isolated drift-orbit resonances, and a chaotic region from overlapping resonances near the trapped-passing boundary.

### 3.2. Classifiers as proxies for collisional losses

A comparison of  $J_{\parallel}$  classifier with the topological classifier shows that the fact that regular orbits are a superset of ideal orbits is mostly reflected. Visually, this means, that the left plots show larger bright yellow regions than the right plots. An exception is seen, e.g. in Fig. 12 in the deeply trapped region. Here, the choice of a relative threshold of 1% in  $J_{\parallel}$  variations breaks down for very short banana orbits and leads to type I errors of this classifier that identify too many orbits as chaotic. This is proven by the topological classifier that identifies mostly ideal orbits in this region, and demonstrates that careful tuning of the  $J_{\parallel}$  classifier is necessary.

The final judgment of the usefulness of the new classifiers and the kind of visualization discussed above is made based on collisionless and collisional direct loss computations in the lower panels of Figs. 7-12. Collisional computations are based on a relatively simple background model of constant temperature  $T = 10$  keV for all species, and electron density of  $n_e = 10^{14} \text{ cm}^{-3}$  in a fusion plasma with a 50:50 D-T mixture. The left plots show the distribution of collisional alpha particle losses over time and initial  $J_{\perp}$ . The right plots show the final lost energy fraction of collisional and collisionless computations. In all tested configurations, the loss channels of chaotic/non-ideal and promptly lost alpha orbits are reflected in the distribution of losses over  $J_{\perp}$ .

## 4. Conclusion

Collisionless and collisional fusion alpha losses in stellarators are prevented by regular phase-space regions acting as radial barriers. Transitions between trapping classes and overlap of drift-orbit resonances introduce chaotic regions that act as loss channels. Overlap of resonances leads to chaotic ripple-induced losses in a similar manner for tokamaks. This analogy is seen in quasi-axisymmetric configurations and is expected to hold also in other quasi-symmetric as well as quasi-isodynamic devices. Relevant regions in phase-space can be efficiently charted by massive classification runs in SIMPLE after



1% of the tracing time of a direct computation of loss fractions. In contrast to their superset of regular orbits that can also produce island-chains in phase-space, ideal orbits correspond to KAM surfaces that are more robust to perturbations. Ideal orbits are a natural generalization of closed  $J_{\parallel}$  contours (Gori *et al.* 1996). They can be identified at similar computational cost by the presented topological classifier without manual adjustments. We therefore propose to use the fraction of ideal orbits on a selection of flux surfaces as a metric for stellarator optimization.

## Acknowledgements

The authors thank Per Helander, Matt Landreman, Joaquim Loizu, Mikhail Mikhailov and Elisabeth Paul for magnetic equilibria and useful discussions, together with the teams of the EUROfusion TSVV task 12 on Stellarator Optimization and the Simon's Collaboration on Hidden Symmetries and Fusion Energy. This work has been carried out within the framework of the EUROfusion Consortium, funded by the European Union via the Euratom Research and Training Programme (Grant Agreement No 101052200 — EUROfusion). Views and opinions expressed are however those of the author(s) only and do not necessarily reflect those of the European Union or the European Commission. Neither the European Union nor the European Commission can be held responsible for them. We gratefully acknowledge support from NAWI Graz. The present contribution is supported by the Helmholtz Association of German Research Centers under the joint research school HIDSS-0006 "Munich School for Data Science - MUDS".

## REFERENCES

- ALBERT, C. G., HEYN, M. F., KAPPER, G., KASILOV, S. V., KERNBICHLER, W. & MARTITSCH, A. F. 2016 Evaluation of toroidal torque by non-resonant magnetic perturbations in tokamaks for resonant transport regimes using a Hamiltonian approach. *Phys. Plasmas* **23** (8), 082515.
- ALBERT, C. G., KASILOV, S. V. & KERNBICHLER, W. 2020*a* Accelerated methods for direct computation of fusion alpha particle losses within, stellarator optimization. *Journal of Plasma Physics* **86** (2), 815860201.
- ALBERT, C. G., KASILOV, S. V. & KERNBICHLER, W. 2020*b* Symplectic integration with non-canonical quadrature for guiding-center orbits in magnetic confinement devices. *J. Comput. Phys.* **403**, 109065.
- ALBERT, C. G., RATH, K., BUCHHOLZ, R., KASILOV, S. V. & KERNBICHLER, W. 2022 Resonant transport of fusion alpha particles in quasisymmetric stellarators. *J. Phys. Conf. Series, Joint Varenna-Lausanne International Workshop* **2397**, 012009.
- CHIRIKOV, BORIS V 1979 A universal instability of many-dimensional oscillator systems. *Physics Reports* **52** (5), 263–379.
- DREVLAK, M., BEIDLER, C. D., GEIGER, J., HELANDER, P., HENNEBERG, S., NÜHRENBURG, C. & TURKIN, Y. 2018 New results in stellarator optimisation. In *27th IAEA Fusion Energy Conf.*, p. 104. IAEA Publications.
- DREVLAK, M., BEIDLER, C. D., GEIGER, J., HELANDER, P. & TURKIN, Y. 2014 Quasi-Isodynamic Configuration with Improved Confinement. In *41st EPS Conf. Plasma Phys.*, p. P1.070.
- GOODMAN, ALAN, MATA, KATIA CAMACHO, HENNEBERG, SOPHIA A., JORGE, ROGERIO, LANDREMAN, MATT, PLUNK, GABRIEL, SMITH, HAKAN, MACKENBACH, RALF & HELANDER, PER 2022 Constructing precisely quasi-isodynamic magnetic fields, arXiv: 2211.09829.
- GORI, S, LOTZ, W & NÜHRENBURG, J 1996 Quasi-isodynamic stellarators. *Theory of Fusion Plasmas (International School of Plasma Physics), Bologna: SIF* p. 335.
- HASTIE, R. J., TAYLOR, J. B. & HAAS, F. A. 1967 Adiabatic invariants and the equilibrium of magnetically trapped particles. *Annals of Physics* **41** (2), 302–338.

- HENNEBERG, S. A., DREVLAK, M., NÜHRENBURG, C., BEIDLER, C. D., TURKIN, Y., LOIZU, J. & HELANDER, P. 2019 Properties of a new quasi-axisymmetric configuration. *Nucl. Fusion* **59** (2), 026014.
- KAMATH, CHANDRIKA 2022 Classification of orbits in Poincaré maps using machine learning. *Int J Data Sci Anal* p. 2346.
- LANDREMAN, M., BULLER, S. & DREVLAK, M. 2022 Optimization of quasi-symmetric stellarators with self-consistent bootstrap current and energetic particle confinement. *Phys. Plasmas* **29** (8), 082501.
- LANDREMAN, M. & PAUL, E. J. 2022 Magnetic Fields with Precise Quasisymmetry for Plasma Confinement. *Phys. Rev. Lett.* **128** (3), 035001.
- PAUL, E. J., BHATTACHARJEE, A., LANDREMAN, M., ALEX, D., VELASCO, J.-L. & NIES, R. 2022 Energetic particle loss mechanisms in reactor-scale equilibria close to quasisymmetry. *Nucl. Fusion* **62** (12), 126054.
- SUBBOTIN, A. A., MIKHAILOV, M. I., SHAFRANOV, V. D., ISAEV, M. YU, NÜHRENBURG, C., NÜHRENBURG, J., ZILLE, R., NEMOV, V. V., KASILOV, S. V., KALYUZHNYJ, V. N. & COOPER, W. A. 2006 Integrated physics optimization of a quasi-isodynamic stellarator with poloidally closed contours of the magnetic field strength. *Nucl. Fusion* **46** (11), 921–927.
- VELASCO, J. L., CALVO, I., MULAS, S., SÁNCHEZ, E., PARRA, F. I., CAPP, Á & TEAM, THE W7-X. 2021 A model for the fast evaluation of prompt losses of energetic ions in stellarators. *Nucl. Fusion* **61** (11), 116059.